Original paper

Simulation of Stress Tests Using a Poroelastic Model to Estimate the Permeability Behavior of Bedford Limestone Samples

Mario E. Vadillo-Sáenz[1], Martín A. Díaz-Viera*, Aarón Domínguez-Torres[1], Enrique Serrano-Saldaña[1] and Manuel Coronado[1]

Resumen

Por su relevancia en Geociencias, el efecto de los esfuerzos sobre las propiedades de flujo de fluido en rocas ha sido estudiado experimental y teóricamente por varias décadas. Los trabajos se han orientado principalmente a rocas tipo arenisca, y relativamente poco, a pesar de su relevancia, en rocas carbonatadas. Por otro lado, la descripción del fenómeno es matemática y numéricamente complejo, ya que involucra el acoplamiento no lineal del flujo de fluido con la deformación de la roca. En este trabajo se busca incursionar en esa parte poco explorada de pruebas experimentales en carbonato y su simulación numérica. En él se presentan pruebas experimentales realizadas en núcleos de caliza Bedford, y se analiza el efecto de los esfuerzos de confinamiento y de la presión del fluido (presión de poro) sobre la permeabilidad a través de dos tipos de pruebas, conocidas como hidrostáticas (bajos esfuerzos de corte) y no hidrostáticas (altos esfuerzos de corte). En este trabajo se presenta un modelo matemático para describir el fenómeno, considerando un fluido monofásico, una respuesta elástica de la roca, y su implementación numérica en elementos finitos. El acoplamiento del flujo de fluido con los esfuerzos se modela utilizando relaciones algebraicas de porosidad y permeabilidad en función del esfuerzo. La relación permeabilidad-esfuerzo utilizada en este trabajo depende linealmente de la deformación volumétrica y la presión de poro. Los resultados experimentales muestran que en general la permeabilidad se incrementa con la presión del fluido y se reduce con el esfuerzo de confinamiento. La reducción con el esfuerzo de confinamiento en el rango de esfuerzos de confinamiento analizado es relativamente pequeña, pero es notoriamente más importante en las pruebas no-hidrostáticas (8%) que en las hidrostáticas (2%). El ajuste del modelo a los resultados experimentales, específicamente a la caída de presión en el núcleo en función del tiempo, se realiza mediante la variación de los parámetros de la relación permeabilidad-esfuerzo. El valor de estos parámetros de ajuste difiere del valor reportado para areniscas, lo cual puede ser indicativo de la diferencia en la estructura porosa y las propiedades mecánicas de las rocas.

Palabras Clave: simulación, poroelasticidad, prueba de esfuerzo y permeabilidad.

---

*Corresponding author at mdiazv@imp.mx
[1]Instituto Mexicano del Petróleo (IMP)Eje Central Lázaro Cárdenas Norte
152, San Bartolo Atepehuacan, Gustavo A. Madero, Ciudad de México.

Abstract

Due to its relevance in Geosciences, the stress effect on the dynamic rock properties has been studied experimentally and theoretically for several decades. These works have been oriented mainly to sandstones, and relatively few to carbonate rocks, despite its relevance. On the other hand, the description of the phenomenon is mathematically and numerically complex since it involves the non-linear coupling of the fluid flow with the rock deformation. This work seeks to analyze that little-explored part of experimental tests in carbonates com bined with its numerical simulation. It presents experimental tests carried out on Bedford limestone cores and analyzes the effect of confinement stress and fluid pressure (pore pres sure) on its permeability, by two test types, known as hydrostatic (low shear stress) and not hydrostatic (high shear stress) tests. In this work, a mathematical model is presented to describe the phenomenon, considering a single-phase fluid, an elastic rock response, and its numerical implementation in finite elements. The coupling of fluid flow with stress is regularly modeled by algebraic relationships of porosity and permeability as a function of stress. A permeability-stress relationship used in this work depends linearly on volumetric strain and pore pressure. The experimental results show that in general, the permeability increases with fluid pressure and decreases with confinement stress. The reduction with the confinement stress is small in the range of confinement stresses analyzed, but it is noticeably more important in the non-hydrostatic tests (8%) than in the hydrostatic ones (2%). The model fitting to experimental data, specifically to the core pressure drop as a function of time, is carried out through the variation of the permeability-stress relationship parame ters. The fitting parameters value differs from the reported value for sandstones, which may be indicative of the difference in the porous structure and mechanical properties of the rocks.

Key words: simulation, poroelasticity, stress test and permeability

NOMENCLATURE	A	Core cross-sectional area $[L^2]$
	c_o	Storage coefficient $[M^{-1} LT^2]$
	c_f	Fluid compressibility $[M^{-1} LT^2]$
	c_s	Solid grain compressibility $[M^{-1} LT^2]$
	D	Core diameter $[L]$
	E	Drained Young modulus $[ML^{-1} T^{-2}]$
	g	Gravity acceleration $[LT^2]$
	G	Shear modulus $[ML^{-1} T^{-2}]$
	k	Permeability $[L^2]$
	k_o	Initial permeability $[L^2]$
	$\boldsymbol{k}$	Permeability tensor $[L^2]$
	K	Drained bulk modulus $[ML^{-1} T^{-2}]$
	K_s	Bulk modulus solid $[ML^{-1} T^{-2}]$
	L	Core length $[L]$
	Δp	Pressure drop $[ML^{-1} T^{-2}]$
	p	Fluid pressure $[ML^{-1} T^{-2}]$
	p_∂	Pressure at the boundary $[ML^{-1} T^{-2}]$
	p_0	Initial pressure $[ML^{-1} T^{-2}]$
	p_{in}	Inlet pressure $[ML^{-1} T^{-2}]$
	p_{out}	Outlet pressure $[ML^{-1} T^{-2}]$
	q_f	Fluid source term $[T^{-1}]$
	Q_{max}	Maximum flow rate $[L^3 T^{-1}]$
	R	Core radius $[L]$
	R_e	Reynolds number [-]
	t	Time $[T]$
	t_S	Time to reach steady state flow $[T]$
	$\boldsymbol{T}$	Traction $[ML^{-1} T^{-2}]$

	$\boldsymbol{T}_\partial$	Traction at the boundary $[ML^{-1} T^{-2}]$
	$\boldsymbol{u}$	Fluid velocity $[LT^{-1}]$
	u_{in}	Injection flow rate $[L^3 T^{-1}]$
	$\boldsymbol{u}_\partial$	Fluid flow at the boundary $[LT^{-1}]$
	V_r	Rock volume $[L^3]$
	ω	Displacement $[L]$
	ω_δ	Displacement at the boundary $[L]$
	ω_0	Initial displacement $[L]$
	W_d	Core dry weight $[M]$

GREEK	α	Biot-Willis coefficient [-]
	β_1, β_2	Permeability fitting parameters [-]
	ε_v	Volumetric strain [-]
	λ	First Lamé constant $[ML^{-1} T^{-2}]$
	μ	Fluid viscosity $[ML^{-1} T^{-1}]$
	ν	Drained Poisson ratio [-]
	ϕ	Porosity [*fraction*]
	ϕ_0	Initial Porosity [*fraction*]
	ρ	Fluid density $[ML^{-3}]$
	ρ_e	Effective density $[ML^{-3}]$
	ρ_s	Solid density $[ML^{-3}]$
	$\sigma_1, \sigma_2, \sigma_3$	Main stresses $[ML^{-1} T^{-2}]$
	$\boldsymbol{\sigma}_c$	Confining stress $[ML^{-1} T^{-2}]$
	$\boldsymbol{\sigma}_e$	Effective stress $[ML^{-1} T^{-2}]$
	σ_T	Total stress $[ML^{-1} T^{-2}]$
	Ω	Simulation domain

INTRODUCTION

The behavior of saturated rocks under stress changes has been a recurring issue in several areas given the importance of knowing and predicting, for example, future production scenarios of a reservoir, storage of residual gas, basin subsidence, etc. The importance lies in the fact that, the coupling between fluid flow and mechanical behavior impacts the flow capacity of the porous medium as a consequence of the stress on its porous structure, altering the porosity and permeability of the rock. In oil reservoirs, it has been found that oil recovery can be importantly overestimated if the geomechanical effects are neglected (Ojagbohunmi *et al.* (2012).

Diverse publications on rock geomechanics have been devoted to experimentally analyze the stress-fluid coupling due to stresses in poroelastic media under diverse conditions (among others, Brace (1965), Jones and Smart (2002), Ma *et al.* (2012), Huo and Benson (2016), Han *et al.* (2016) and Belmokhtar *et al.* (2017)), and to analyze the permeability dependence on applied stress (Zhu *et al.* (1997), Zhu and Wong (1997), Lion *et al.* (2004), Fortin *et al.* (2005), Al-Quraishi *et al.* (2010), Takahashi *et al.* (2013) and Wang *et al.* (2016)). Simultaneously, other works have developed poroelastic models to mathematiccally describe the stress effects on permeability (Mandel (1953), Abousleiman *et al.* (1996), Cui and Abousleiman (2001) and Lamb and Gorman (2010)), and have also proposed empirical and theoretical correlations of the porosity and permeability dependence on stress and pore pressure (Kozeny (1927), Carman (1956), Walder and Nur (1984), David *et al.* (1994),Touhidi-Baghini (1998), Mainguy and Longuemare (2002) and Ma (2015)). Also, some few numerical simulations of this flow-stress coupling in homogeneous and fractured rocks have also been published (Bai *et al.* (1997), Rinaldi and Rutqvist (2016), Roded and Holtzman (2017), Agheshlui *et al.* (2018), Goral *et al.* (2020) and Sasaki and Rutqvist (2021)). Some of the conclusions are in general, that permeability changes result from a competetion between two mechanisms, (i) rock structure compaction that increases tortuosity and causes a decrease in permeability, and (ii) dilation of voids, that increases pore volume and increments permeability (Jones and Smart, 2002; Han *et al.*, 2016). The presence of micro-fractures and large fractures in the rock can also importantly impact permeability response to stresses (Barthelemy, 2009).

Despite of its relevance, only few of the published experimental works consider carbonate rocks, and only few of them apply mathematical and numerical models to analyze and describe the observed permeability results as function of confinement stress. This work analyzes that little-explored part of experimental tests on carbonate rocks combined with their numerical simulation using a permeability-stress relationship linearly dependent on volumetric strain and pore pressure.

The paper is organized as follows. In the first section an introduction and a literature review is provided. In the second section a description of the experimental setup, the laboratory tests and the test results are given. In the third section, the poroelastic model is presented including the mathematical formulation, the initial and boundary conditions, the numerical discretization and its computational implementation. In the fourth section the application of the model to the hydrostatic and non-hydrostatic experimental tests is shown. In this section, also a comparison between the numerical simulation and the permeability experimental results is presented. The concluding remarks are shown in the last section.

EXPERIMENTAL SETUP

The Bedford limestone samples employed in this study (see Fig. 1) were characterized by X-ray diffraction analysis (XDR), X-ray micro-tomography and geomechanical testing. Their composition is 97 %w calcium carbonate and 3 %w silicon oxide. They have an average effective porosity of 13.8 %, a pore throat size in the range of 40-52 μm, very irregular grain shapes with grain density of 2,711 kg/m³, a drained Young modulus (E) of 16.1 GPa, and a drained Poisson ratio (v) of 0.15 (Coronado, 2019).

Figure 1. Bedford limestone sample used in this work.

The permeability study was performed in two cylindrical samples (A and B) which were cored from a Bedford limestone block. The dimensions and physical properties of the cores are shown in Table 1. The displacement fluid used in the test was distilled water in order to prevent pore obstruction due to scale formation and deposition, and also to avoid calcite dissolution.

Traditionally, Hoek and Hassler coreholders are used in laboratory to measure dynamical properties as function of the rock mechanical properties. Instrumented Hoek triaxial coreholders can handle independently axial and confining (radial) stress and allow strain measurements in both radial and axial directions (Hoek and Franklin, 1968). In contrast, Hassler coreholders used in SCAL testing (McPhee *et al.*, 2015) (Figure 2) can work in two possible test configurations: hydrostatic and non-hydrostatic. In the first case the radial confining stress equals the stress on the sample endfaces. On the other hand, in the second case, the radial confining stress differs from the endface stress. Sample A was employed in the non-hydrostatic tests, and sample B in the hydrostatic ones. Here, for evaluating stress effects on samples permeability a Hassler coreholder was used. The core is loaded in a Viton rubber sleeve and its endfaces are set in contact with the stainless steel difusser at each end. These are attached to the inlet and outlet fluid lines.

Table 1. Physical properties of the Bedford limestone samples.

Property	Dimensions	Bedford A	Bedford B
Core length (L)	m	0.127	0.123
Core diameter (D)	m	0.1016	0.1016
Porosity (ϕ)	%	13.6	14.0
Permeability (k)	m²	1.51×10^{-13}	1.23×10^{-13}
Core cross-sectional area (A)	m²	8.17×10^{-3}	8.17×10^{-3}
Rock volume (V_r)	m³	1.03×10^{-3}	1.00×10^{-3}
Core dry weight (W_d)	kg	2.25	2.18

The fluid displacement system is composed by a Quizix pump Q5000, a back pressure regulator (BPR) controlled by a Teledyne Isco 260D syringe pump, pressure and temperature sensors and a National Instruments data acquisition unit. The pressure sensors measure the pressure at the sample endfaces, and the differential pressure transducer measures the pressure drop across the sample. The temperature sensor was set at coreholder body. The data adquisition system was programmed in LabVIEW 2018. A schematic view of the displacement system is shown in Figure 3.

The confining stress was applied by pressurizing the hydraulic fluid (distilled water) between the wall of the coreholder and the Viton sleeve. This confining stress was servo controlled by the Quizix pump. The Viton sleeve used to seal the sample was capable of withstanding a maximum confining pressure of 27.5 MPa without rupture. The sample pore pressure was set by pressurizing distilled water inside the sample, controlled by the BPR. A clean and dry sample covered by the viton rubber was set in the coreholder. After assembling the system and calibrating the pressure and temperature sensors, all the fluid lines together with the sample was air evacuated for 45 min.

Following the standard method, the sample was saturated at a confining stress (σ_c) of 13.8 MPa and at a room temperature (295 K). A constant flow rate of 0.1 ml/min was applied until the inlet pressure (p_{in}) reaches a plateau (approximately after 48 h) at 6.9 MPa. The resulting differential pressure (σ_c-p_{in}) of 6.9 MPa was enough to avoid core-sleeve interface flow and provides a seal between the sleeve and the coreholder.

The initial connected porosity was calculated from the saturated sample density, by considering distilled water and the rock matrix densities (Ramos da Silva *et al.* (2010). The resulting porosity values are 13.6 % and 14.0 % for A and B samples, respectively.
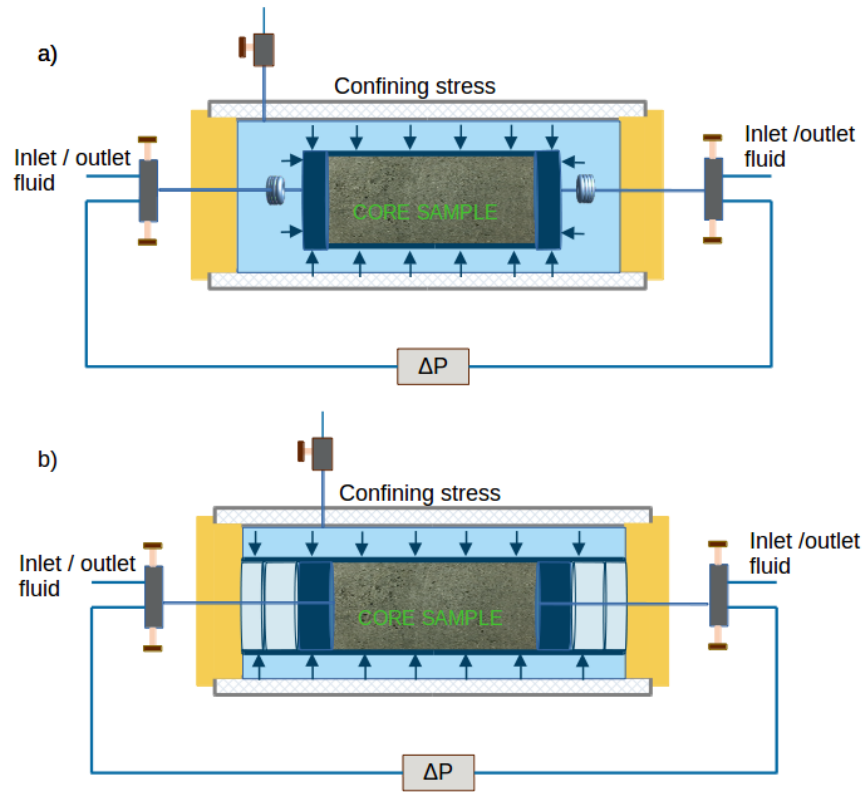

Figure 2. a) Hydrostatic and b) non-hydrostatic coreholder configurations.
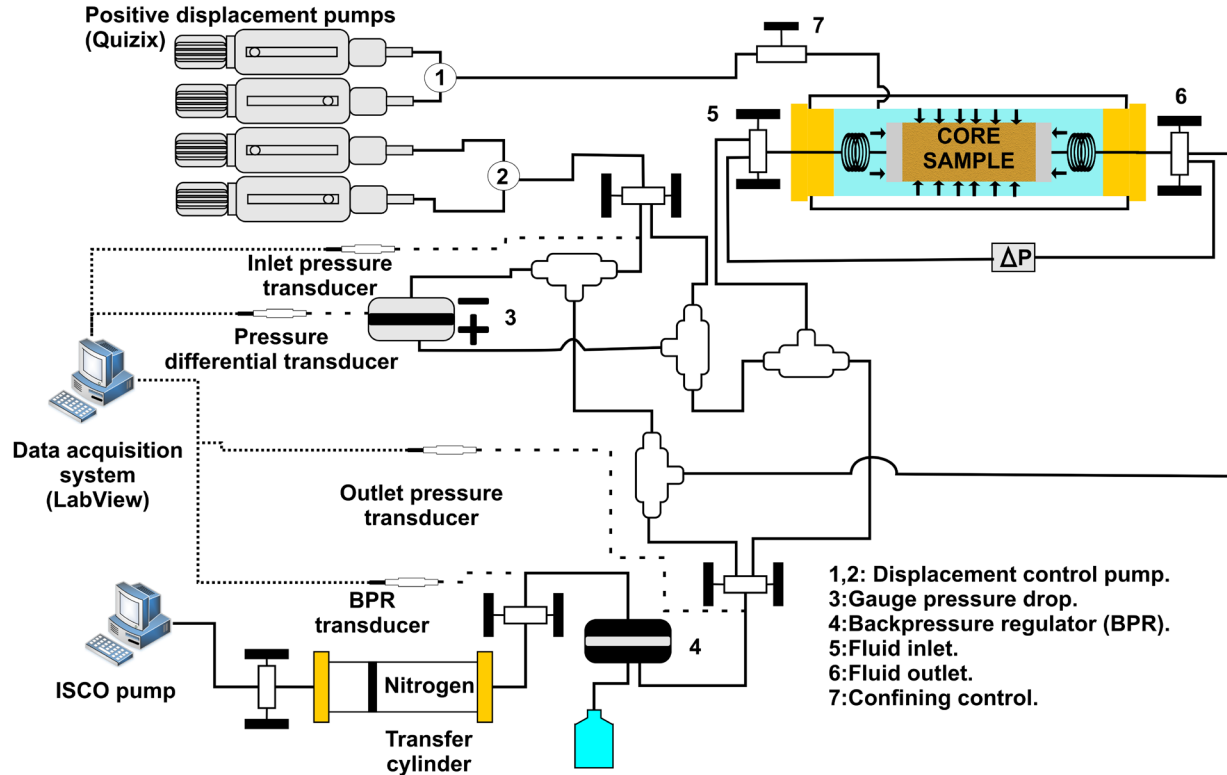
Figure 3. Displacement system scheme.

Four permeability tests on samples A and B were carried out using the steady state method at constant flow rate (1, 2, 3 and 4 ml/min). The pressure drop was used to evaluate the permeability by the Darcy's law. The laminar flow assumption behind Darcy's law (Glowacki and Seladurai (2016) Selvadurai and Selvadurai (2010) holds, since the estimated maximum interstitial fluid velocity is 5×10^{-5} m/s, which corresponds to a maximum Reynolds number (R_e) of 0.003, and satisfies the Philips (1991) condition $R_e < \phi$, and Bear (1972) condition $R_e < \phi$. The permeability values obtained at these confining stresses are 1.51×10^{-13} m² and 1.23×10^{-13} m² for A and B samples, respectively.

In the non-hydrostatic test, the outlet pressure was controlled by the BPR and the inlet pressure was set by the Quizix pump at constant pressure (6.9 MPa), that is achieved by adjusting its flow rate. The axial stress equals the atmosferic pressure and the boundary condition at the core sample axial faces is zero displacement (see Figure 4). The experiment starts with the application of a series of confining stress for a time period of 40 min. During this time, the inlet and outlet pressures, the pressure drop, the confining pressure, the injected and recovered fluid volumes and the temperature were recorded. These tests are carried out for eight confining stresses as shown in Table 2.

The hydrostatic tests have the same boundary conditions as the non-hydrostatic tests, with the only difference being that the axial confining stress and radial confining stress are the same. In a similar way, these tests are carried out for six confining stresses as shown in Table 3.

The permeability results for non-hydrostatic and hydrostatic tests are presented in Table 2 and Table 3, respectively.

Table 2. Mean and standard deviation of permeability ($\times 10^{-15}$ m^2) data for non-hydrostatic tests.

Pore Pressure	Confining stress (MPa)							
(MPa)	9.7	11.0	12.4	13.8	19.3	22.1	24.8	27.6
6.9	111±0.3	139±0.2	138±0.2	138±0.3	133±0.2	134±0.2	130±0.2	127±0.3

Table 3. Mean and standard deviation of permeability ($\times 10^{-15}$ m^2) data for hydrostatic tests.

Pore Pressure	Confining stress (MPa)					
(MPa)	3.4	6.9	10.3	13.8	20.7	27.6
2.1	108±0.3	109±0.3	108±0.3	108±0.3	107±0.4	106±0.3

POROELASTIC MODEL

This model describes a single phase flow of a slightly compressible fluid in a porous medium with linear elastic deformation (Díaz-Viera *et al.* (2020)). The rock deformation is described by a quasi-steady state moment equilibrium equation. The influence of the fluid is explained through the concept of effective stress due to Terzaghi (1923, 1925) and Biot (1941, 1955). The total stress acting on a porous medium is supported by both the solid matrix and the saturating fluid. The effective stress represents the part of the total stress supported by the solid matrix and can be determined as a function of deformation.

The model considers an isothermal system composed by one fluid and one solid, each consisting of a single component. The solid phase is a deformable porous medium fully saturated by the fluid, which is assumed Newtonian. Both, fluid and solid are slightly compressible. The solid phase is at rest, only displacements caused by mechanical stresses are present. Also, the solid has a linear elastic behavior and satisfies the Hooke's law for its constitutive stress-strain relationship.

The poroelasticity equation system consist of a momentum and a mass balance equation derived by Biot (1941, 1955). Here the model formulation follows Showalter (2000) notation. The monophasic flow model corresponds to a deformable linear elastic porous medium and it is formulated by Biot (1955); Chen *et al.* (2004).

$$\frac{\partial}{\partial t}(c_0 p + \alpha \nabla \cdot \omega) - \nabla \left(\frac{k}{\mu} \cdot \nabla p + \rho g \nabla z \right) = q_f \quad , \tag{1}$$

where c_0 is the storage coefficient, p is the fluid pressure, also known as pore pressure, α is the Biot-Willis coefficient (Biot and Willis (1957)) with $0 \leq \alpha \leq 1$, $\boldsymbol{\omega}$ is the displacement vector, $\boldsymbol{k}$ is the permeability tensor, μ is the fluid viscosity, ρ is the fluid density, g is the gravity acceleration, z is the elevation and q_f is the fluid source term.

The storage coefficient c_0 is defined as

$$c_0 = (\alpha - \phi)\ c_r + \phi c_f \tag{2}$$

where ϕ is the porosity, c_r is the solid grain compressibility and c_f is de fluid compressibility.

The quasi-stationary momentum balance equation for a porous medium saturated with a fluid is

$$-\nabla \cdot (\sigma_e - \alpha p \mathbf{I}) = \rho_e g \nabla z \tag{3}$$

where $\sigma_T = \sigma_e - \alpha p \mathbf{I}$ is the total stress tensor and σ_e is the effective stress tensor. While ρ_e is an effective density defined as $\phi\rho + (1-\phi)\rho_s$, being ρ_s the rock density.

In particular, the effective stress tensor according to Hooke's law for the linear homogenous and isotropic case can be expressed as

$$\sigma_e = (\lambda + G)\nabla(\nabla \cdot \omega) + G\nabla^2 \omega \tag{4}$$

where G and λ are the shear modulus and first Lamè constant, respectively. Note that the porosity and the absolute permeability tensor can be function of pore pressure (p), displacements (ω), volumetric strain (ε_v) or other quantities. Here, the solid mechanics sign convention is considered, which means that compressive stresses are negative and tensile stresses are positive.

The poroelasticity problem consists in solving Eqs. (1) and (3), and the unknowns are pore pressure (p) and the displacement (ω). The initial and boundary conditions are

Initial conditions

$$p(x,t_0) = p_0(x), \quad \forall x \in \Omega, \quad t = t_0 \tag{5}$$

$$\omega(x,t_0) = \omega_0(x), \quad \forall x \in \Omega, \quad t = t_0 \tag{6}$$

where p_0 and w_0 are initial values for pore pressure and displacement, respectively.

Boundary conditions

$$\omega(x,t) = \omega_\partial(x,t), \quad \forall x \in \partial_D^\omega \Omega \quad t > t_0 \tag{7}$$

$$\sigma_T(x,t) \cdot n = T_\partial(x,t), \quad \forall x \in \partial_D^\omega \Omega \; t > t_0 \tag{8}$$

$$p(x,t) = p_\partial(x,t), \quad \forall x \in \partial_D^p \Omega \; t > t_0 \tag{9}$$

$$u(x,t) \cdot n = u_\partial(x,t) \cdot n, \quad \forall x \in \partial_N^p \Omega \quad t > t_0 \tag{10}$$

where ω_∂, T_∂, p_∂ and u_∂ are displacement, traction, pressure and fluid flow at the boundary, respectively. Here, Ω is a bounded domain with boundary $\partial\Omega$ formed by two parts, one with Dirichlet conditions $\partial_D\Omega$ and the other with Neumann conditions $\partial_N\Omega$, where $\partial\Omega = \partial_D\Omega \cup \partial_N\Omega$ and $\partial_D\Omega \cap \partial_N\Omega = \emptyset$.

The fluid flow is expressed by the Darcy's law

$$u = -\frac{k}{\mu} \cdot (\nabla p + \rho g \nabla z)$$

(11)

where u is the Darcy velocity.

The numerical model is implemented using the module *PDE, Coefficient Form* in COMSOL Multiphysics (2018).

NUMERICAL SIMULATIONS

In this section, the numerical simulations of two case studies corresponding to non-hydrostatic and hydrostatic compression tests are presented. In both cases, the effect of the stresses on the petrophysical properties (permeability and porosity) is studied. To this purpose the previous poroelastic model is applied together with constitutive relationships for porosity and permeability in term of stress.

Porosity-stress relationship

Here, the porosity as a function of stress, proposed by Mainguy and Longuemare (2002) and described by Coussy (2004) is used. It provides a porosity relationship in terms of the volumetric strain (ε_v) and pore pressure (p) as follows

$$\phi = \phi_0 + \alpha(\varepsilon_v - \varepsilon_{v0}) + c_s (\alpha - \phi_0)(p - p_0)$$

(12)

where ϕ_0, ε_{v0} and p_0 are initial porosity, volumetric strain and pore pressure, respectively.

Permeability-stress relationship

The permeability-stress relationship used in this work is given in terms of volumetric strain (ε_v) and pore pressure (p), as follows

$$k = k_0 [1 + \beta_1 (\varepsilon_v - \varepsilon_{v0}) + \beta_2 (p - p_0)]$$

(13)

where k_0, ε_{v0} and p_0 are initial permeability, volumetric strain and pore pressure, respecttively, and β_1 and β_2 are fitting parameters as in the previous work by Vadillo-Sáenz *et al.* (2020a), where it was shown that the frequently used permeability relationships can be approximated by a linear stress relationship. Accordingly, porosity and permeability, in Eq. (12) and (13) are linear functions of volumetric strain and pore pressure, respectively.

It should be mentioned that the fluid compressibility (c_f), fluid density (ρ), solid density (ρ_s), maximum flow rate (Q_{max}), bulk modulus solid (K_s), drained Young modulus (E), drained Poisson's ratio (ν), Biot-Willis coefficient (α), rock compressibility (c_s), drained bulk modulus (K), first Lamé constant (λ) and shear modulus (G) are all kept constant during the numerical simulation.

In the Figure 4 a schematic representation of the boundary conditions for the hydrostatic and non-hydrostatic tests are shown.

All equations are discretized using a standard finite element method in space, and the Euler's backward finite difference method for time discretization, what gives place to a fully implicit scheme.
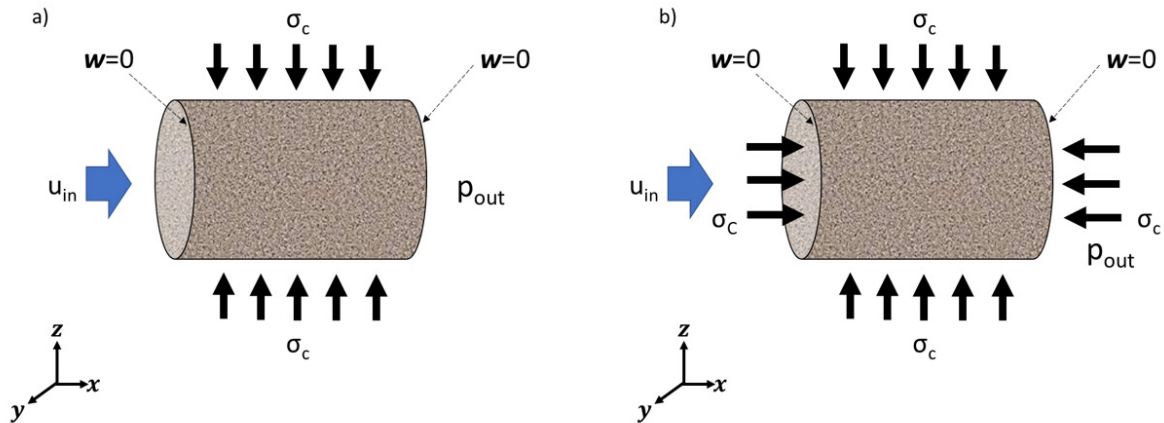
Figure 4. Schematic view of the boundary conditions: (a) the non-hydrostatic case, where $\omega_r = \omega_x = 0$ at the end faces and (b) the hydrostatic case, where $\omega_r = 0$ at the end face. Fluid is injected at constant flow rate from the left side, while pressure is set constant at the right side.

The finite element method is applied by using quadratic Lagrange elements in an unstructured triangular/tetrahedral mesh in 2D/3D. The resulting linear algebraic system is solved by the LU direct method UMFPACK for non symmetric and sparse matrices. The Newton-Raphson method is applied when the problem becomes non-linear.

The numerical model was implemented in COMSOL Multiphysics (COMSOL Multiphysics, 2018) and it was validated by comparing the numerical solution with the anaytical solution of the classical Mandel consolidation problem (Mandel, 1953; Abousleiman *et al.*, 1996). A more datailed description of the problem and its validation are given in Vadillo-Sáenz *et al.* (2020a).

Case study A: Non-hydrostatic Compression Tests Simulation.

The initial conditions for pore pressure is set equal to the outlet pressure ($p_0 = p_{out}$) and zero for displacement ($\omega_0 = 0$), respectively. The core is subjected to a constant pore pressure of 6.9 MPa and the radial confining stress sequence shown in Table 2, each for a time period of 40 min. The left and right sides are fixed, i.e. non-displacement in both radial and axial directions.

The problem is solved numerically by considering a 3D cylindrical domain with radius R = 0.051 m and length L=0.127 m as displayed in Figure 4 and Table 1. The domain is partitioned by an unstructured mesh of 2,420 tetrahedral elements. The simulation data for the non-hydrostatic compression tests are given in the Table 4.

On evaluating permeability by Eq. (13) each confinement stress, a fitting procedure to match the experimental pressure drop was carried out. The parameter β_1 best fit value is 30 with a very little variation in a range of ±5, while the parameter β_2 is practically insensitive with a best fitting value of 1×10^{-8} Pa^{-1} for all cases. Figure 9 in Appendix A shows the best fit obtained at each confining stress for non-hydrostatic compression tests.

The porosity and permeability simulation results for the non-hydrostatic compression tests are displayed in Figures 5 and 6, respectively. The porosity change (Figure 5) corresponds to the physically

expected behavior when subjecting a core to increasing confining stress. A reduction of approximately 1% of the porosity in the core is shown. It is important to notice that no measurements of porosity were made, it is only evaluated through Eq. (12). It could be observed in Figure 6 that the general trend shows the expected behavior of a core subjected to a increased confining stress except for the value at confining stress 19.3 MPa. It is also seen in Figure 6 that all numerical results (brown diamonds) fall within the boxplot of each test except in the aforementioned point. A core permeability reduction of approximately 8% at the end of the non-hydrostatic compression tests is observed. The simulated permeability values versus the experimental data give an acceptable RMS fitting error of 0.125.

Table 4. Non-hydrostatic compression tests data. Asterisk (*) means that the median value of the equilibrium flow rate was taken.

Parameter	Value	Unit
Fluid compressibility (c_f)	4×10^{-10}	1/Pa
Fluid density (ρ)	1000	kg/m^3
Solid density (ρ_s)	2530	kg/m^3
Confining stress (σ_c)	12.4	MPa
Maximum flow rate (Q_{max})	15	ml/min
Bulk modulus solid (K_s)	14.4	GPa
Drained Young modulus (E)	16.1	GPa
Initial porosity (ϕ_0)	13.63	%
Initial permeability (k_0)	1.39×10^{-13}	m^2
Outlet pressure (p_{out})*	6.67	MPa
Drained Poisson's ratio (v)	0.15	-
Coreholder temperature	295.78	K
Time to reach flow steady state Q_{max} (t_s)	20	min
Fluid viscosity (μ)	9.4×10^{-4}	Pa·s
Biot-Willis coefficient (α)	0.47	-
Rock compressibility (c_s)	6.93×10^{-11}	1/Pa
Drained bulk modulus (K)	7.61	GPa
First Lam´e constant (λ)	2.98	GPa
Shear modulus (G)	6.95	GPa

CASE STUDY B: HYDROSTATIC COMPRESSION TESTS SIMULATION

In the hydrostatic case, the in Table 3 given confining stress sequence is applied for 50 min time period while keeping to all sample faces at a constant pore pressure of 2.1 MPa. Both left and right core sides are subjected to a non-displacement condition in the radial direction only ($\omega_r = 0$), the rest of the initial and boundary conditions are the same as in case A. The system domain is a 3D cylinder of radius R = 0.051 m and length L = 0.128 m.

Figure 4 and Table 1. The mesh is made up of 2,440 tetrahedral elements. The values of the parameters that are different from case A are given in the Table 5.

In the same way as in the non-hydrostatic compression tests Eq. 12 was used to estimate the dependence of rock porosity as a function of stress. The final results obtained for the non-hydrostatic
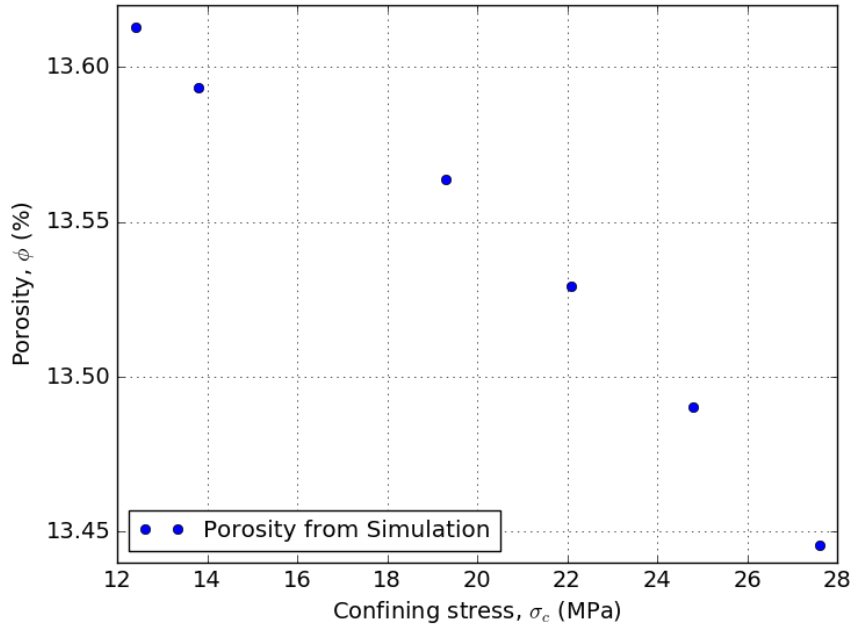
Figure 5. Porosity versus confining stress in case A non-hydrostatic tests.
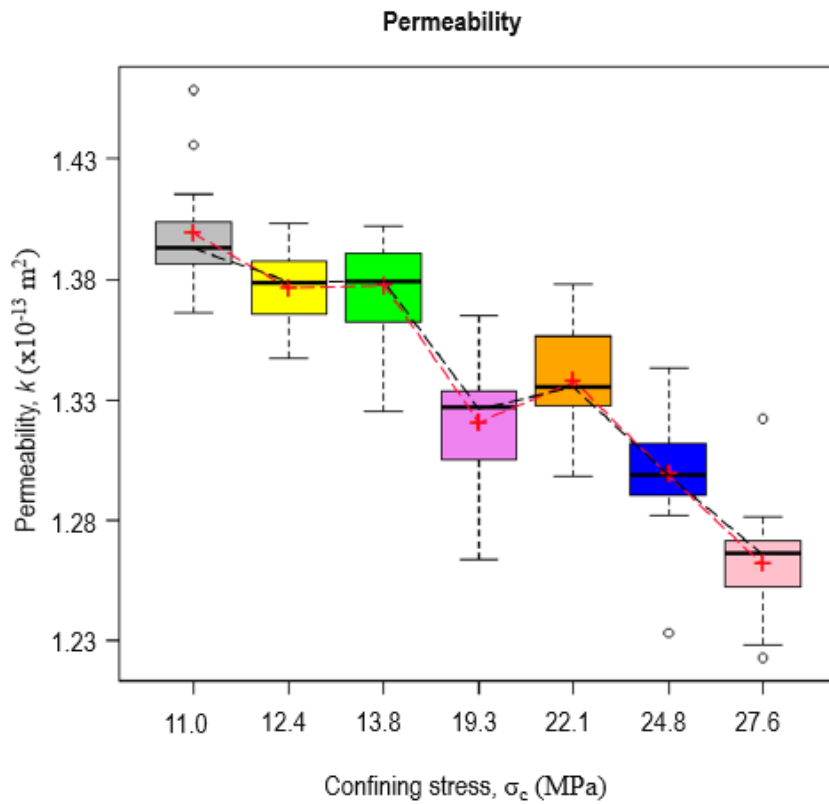
Permeability

Figure 6. Boxplots of permeability versus confining stress in Case A non-hydrostatic tests. The simulation results are displayed as brown diamonds, the median experimental data values are displayed as a black line, and the mean experimental data are displayed as red crosses

Table 5. Hydrostatic compression tests data. Asterisk (*) means that the median value of the equilibrium flow rate was taken.

Parameter	Value	Unit
Solid density (ρ_s)	2634	kg/m³
Confining stress (σ_c)	10.3	MPa
Initial porosity (ϕ_0)	14.02	%
Initial permeability (k_0)	1.09×10^{-13}	m²
Outlet pressure (p_{out})*	1.94	MPa
Coreholder temperature	294.5	K
Time to reach flow steady state Q_{max} (t_s)	36	min
Fluid viscosity (μ)	9.5×10^{-4}	Pa·s

compression tests are displayed in Figure 7. The porosity change shows the physically behavior expected for a core subject to an increasing confinement stress. A reduction of approximately 1% of the porosity in the core is estimated.

The best β_1 fit value is 20 with small variations near ±5. The β_2 parameter is practically insensitive, taking in all cases its best fit value at 1×10^{-8} Pa^{-1}, for all cases. The Figure 10 in Appendix A shows best fit values obtained in the hydrostatic tests.

The results displayed in Figure 8 show the physically expected behavior in a core subjected to an increasing confining stress. No values outside of the general trend appear. A reduction of approximately 2% of the permeability in the core at the end of the hydrostatic tests is observed. A difference between the experimental permeability data and the simulation results of 0.844 RMS error is seen.
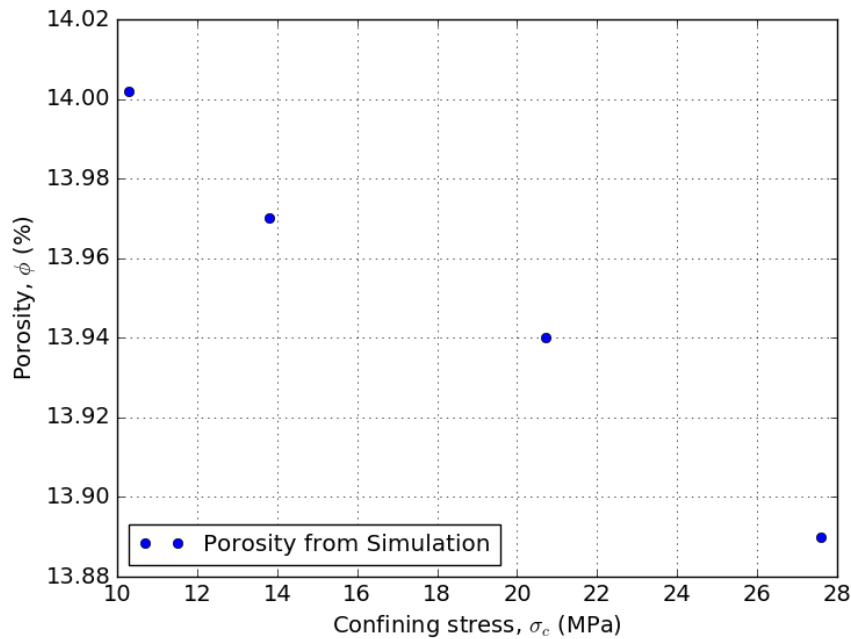

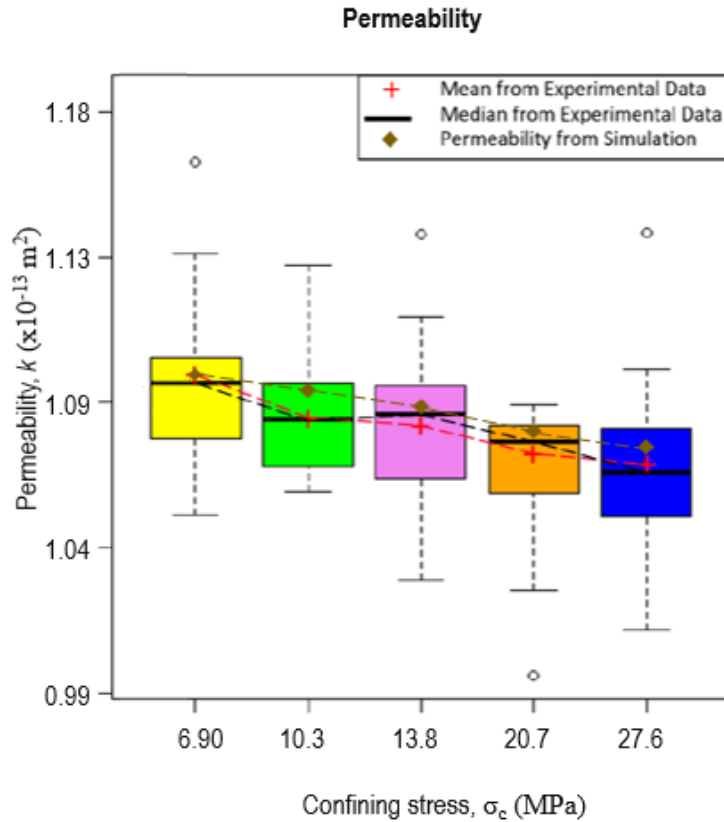Figure 7. Porosity versus confining stress in case B hydrostatic tests.

Permeability

Figure 8. Boxplots of permeability versus confining stress for Case B hydrostatic tests. The simulation results are displayed as brown diamonds, the median experimental data values are displayed as a black line, and the mean experimental data are displayed as red crosses.

CONCLUSIONS

Permeability experimental results in terms of volumetric strain and pore pressure in Bedford limestone cores for hydrostatic (low shear stresses) and non-hydrostatic (high shear stresses) tests, in the elastic range have been here presented. Also, a mathematical model has been shown to describe the effect of the confinement stress on rock porosity and permeability by considering single-phase flow and elastic rock response. The main results and conclusions are:

The literature review shows that multiple experimental results on the effect of confinement stress on permeability in sandstone rocks have been reported, but only few tests in carbonate rocks have been performed, despite its relevance. It was found in the present work, that permeability in Bedford limestone is more sensitive to stress than sandstones.

The effect of stress on permeability is clearly stronger when higher shear stresses are present (non-hydrostatic tests), than when small shear stresses are applied (hydrostatic tests). In the linear confining stress range analyzed, from 10 to 28 MPa, the non-hydrostatic case gives a reduction of 8% (with a pore pressure of 6.9 MPa) and in the hydrostatic case gives place to only 2% (with a pore pressure of 2.1 MPa). The above behavior could be explained by noticing that shear stresses can lead to large pore spaces reductions, probably due to a better rearrangement and closure of the internal porous structure of the Bedford limestone, which is made up of highly irregular grains.

There are very few studies published in the literature in which both experimental tests and numerical simulation results of the change in permeability as a function of stress are presented. For this

purpose, a in-house mathematical and computational model has been developed. The few experimental published tests that include modeling employ, third-party software whose operation and results interpretation is not entirely clear.

The model used to analyze the pressure drop experimental data involves fitting parameters permeability-stress correlation model (Eq. 13). The data fitting achieved has been excellent. This indicates that the mathematical model developed describes adequately the phenomenon.

Based on the results here obtained, this work provides useful information for formulating and validating constitutive models for the flow-stress dependence in homogeneous and isotropic poroelastic media. Larger data fitting differences could be expected when working with deformable fractured porous media.

Acknowledgements

Referencess

Abousleiman, Y., Cheng, A. H.-D., Cui, L., Detournay, E., and Roegiers, J.-C. (1996). Mandel's problem revisited. *Geotechnique*, 46(2):187–195.

Agheshlui, H., Sedaghat, M. H., and Matthai, S. (2018). Stress influence on fracture aperture and permeability of fragmented rocks. *Journal of Geophysical Research: Solid Earth*, 123(5):3578–3592.

Al-Quraishi, A. A., Almisned, O. A., and Al-Awad, M. N. (2010). Relative permeabilities of homogeneous and heterogeneous laminated rock samples under hydrostatic and triaxial stresses. *Journal of King Saud University - Engineering Sciences*, 22(2):101–109.

Bai, M., Meng, F., Elsworth, D., Zaman, Z., and Roegiers, J. (1997). Numerical modeling of stress-dependent permeability. *International Journal of Rock Mechanics and Minings Sciences*, 34(3-4). Proceedings of the 1997 36th US Rock Mechanics ISRM International Symposium ; Conference date: 29-06-1997 Through 02-07-1997.

Barthlmy, J.-F. (2009). Effective permeability of media with a dense network of long and micro fractures. *Transport in Porous Media*, 76:153–178.

Bear, J. (1972). *Dynamics of fluids in porous media.* Environmental science series. Elsevier.

Belmokhtar, M., Delage, P., Ghabezloo, S., Tang, A.-M., Menaceur, H., and Conil, N. (2017). Poroelasticity of the Callovo-Oxfordian Claystone. *Rock Mechanics and Rock Engineering*, 50(4):871–889.

Biot, M. and Willis, D. (1957). The elastic coefficients of the theory of consolidation. *Journal of Applied Mechanics ASME*, 24:594 – 601.

Biot, M. A. (1941). General theory of three-dimensional consolidation. *Journal of Applied Physics*, 12(2):155–164.

Biot, M. A. (1955). Theory of elasticity and consolidation for a porous anisotropic solid. *Journal of Applied Physics*, 26:182 – 185.

Brace, W. F. (1965). Some new measurements of linear compressibility of rocks. *Journal of Geophysical Research* (1896-1977), 70(2):391–398.

Carman, P. C. (1956). *Flow of gases through porous media.* Butterworths Scientific Publications London.

Chen, Z., Lyons, S., and Qin, G. (2004). The mechanical behavior of poroelastic media saturated with a newtonian fluid derived via homogenization. *International Journal of Numerical Analysis and Modeling*, 1:75 – 98.

COMSOL Multiphysics (2018). Reference manual, version 5.4. *COMSOL AB*.

Coronado, M. (2019). Informe Final de la Etapa 2. *Technical Report. Proyect 280097 (IMP Y.61066). Fondo Sectorial Conacyt-Sener-Hidrocarburos, Mexican* Petroleum Institute, Mexico City.

Coussy, O. (2004). *Poromechanics*. John Wiley and Sons, Chichester, England, first edition.

Cui, L. and Abousleiman, Y. (2001). Time-dependent poromechanical responses of saturated cylinders. *Journal of Engineering Mechanics*, 127(4):391–398.

David, C., Wong, T.-F., Zhu, W., and Zhang, J. (1994). Laboratory measurement of compaction-induced permeability change in porous rocks: Implications for the generation and maintenance of pore pressure excess in the crust. *Pure and applied geophysics*, 143:425–456.

Díaz-Viera, M., Aguilar-Gastelum, P., Coronado, M., Vadillo-Sáenz, M., and Wilson- García, E. (2020). Modelo matemático, numérico y computacional de poroelasticidad monofásico. *Internal Report of th Fondo Sectorial Conacyt Sener Hidrocarburos Project 280097 (IMP-Y.61066) October 15, 2020*.

Ferronato, M., Castelletto, N., and Gambolati, G. (2010). A fully coupled 3-d mixed finite element model of biot consolidation. *Journal of Computational Physics*, 229(12):4813 – 4830.

Fortin, J., Schubnel, A., and Guguen, Y. (2005). Elastic wave velocities and permeability evolution during compaction of bleuswiller sandstone. *International Journal of Rock Mechanics and Mining Sciences*, 42:873–889.

Glowacki, A. and Seladurai, A. (2016). Stress-induced permeability changes in indiana limestone. *Engineering Geology*, 215(19):122–130.

Goral, J., Panja, P., Deo, M., Andrew, M., Linden, S., Schwarz, J.-O., and Wiegmann, A. (2020). Confinement effect on porosity and permeability of shales. *Scientific Reports*, 10.

Han, B., Xie, S. Y., and Shao, J. F. (2016). Experimental Investigation on Mechanical Behavior and Permeability Evolution of a Porous Limestone Under Compression. *Rock Mechanics and Rock Engineering*, 49:3425–3435.

Hoek, E. and Franklin, J. (1968). A simple triaxial cell for field and laboratory testing of rock. *Transactions of the Institution of Mining and Metallurgy*, 77:A22–26.

Huo, D. and Benson, S. (2016). Experimental investigation of stress-dependency of relative permeability in rock fractures. *Transport in Porous Media*, 113:567–590.

Jones, C. and Smart, B. (2002). Stress induced changes in two-phase permeability. In *SPE/ISRM Rock Mechanics Conference held in Irving, Texas, 20-23 October*, number SPE/ISRM 78155. Society of Petroleum Engineers.

Kozeny, J. (1927) Über kapillare Leitung des Wassers im Boden, Sitzb. *Akademie der Wissenschaften in Wien. Mathematisch-Naturwissenschaftliche Klasse*, 136:271–306.

Lamb, A. and Gorman, G. (2010). Finite element coupled deformation and fluid flow in fractured porous media. In *SPE EUROPEC/EAGE Annual Conference and Exhibition held in Barcelona, Spain, 1417 June 2010*, number SPE-131725. Society of Petroleum Engineers.

Li, P., Chalaturnyk, R., and Polikar, M. (2004). Issues with reservoir geomechanical simulation of the sagd process. *Journal of Canadian Petroleum Technology*, 43(1):1–11.

Lion, M., Skoczylas, F., and Ledesert, B. (2004). Determination of the main hydraulic and poro-elastic properties of a limestone from bourgogne, france. *International Journal of Rock Mechanics and Mining Sciences*, 41:915–925.

Ma, F., He, S., Zhu, H., Xie, Q., and Jiao, C. (2012). The effect of stress and pore pressure on formation permeability of ultra-low-permeability reservoir. *Petroleum Science and Technology*, 30(12):1221–1231.

Ma, J. (2015). Review of permeability evolution model for fractured porous media. *Journal of Rock Mechanics and Geotechnical Engineering*, 7:351–357. Peer review under responsibility of Institute of Rock and Soil Mechanics, Chinese Academy of Sciences.

Mainguy, M. and Longuemare, P. (2002). Coupling fluid flow and rock mechanics: Formulation of the partial coupling between reservoir and geomechanical simulators. *Oil & Gas Science and Technology*, 57(4):355–367.

Mandel, J. (1953). Consolidation des sols (´etude mathématique). *Geotechnique*, 30:287 – 299.

McPhee, C., Reed, J., and Zubizarreta, I. (2015). *Core Analysis: A Best Practice Guide*. ISSN. Elsevier Science.

Ojagbohunmi, S., Chalaturnyk, R., and Leung, J. (2012). Coupling of stress-dependent relative permeability and reservoir simulation. *In Eighteenth SPE Improved Oil Recovery Symposium held in Tulsa*, Oklahoma, USA, 1418 April 2012.

Philips, O. (1991). Flow and reactions in permeable rocks. *Cambridge University Press*, Cambridge, UK.

Ramos da Silva, M., Schroeder, C., and Verbrugge, J.-C. (2010). Poroelastic behavior of a water-saturated limestone. *International Journal of Rock Mechanics and Mining Sciences*, 47:797–807.

Rinaldi, A. P. and Rutqvist, J. (2016). Modeling stress/strain-dependent permeability changes for deep geoenergy applications. In *EGU General Assembly Conference Abstracts*, EGU General Assembly Conference Abstracts, pages EPSC2016–15108.

Roded, R. and Holtzman, R. (2017). Reactive transport under stress: Permeability evolution by chemo-mechanical deformation. In *AGU Fall Meeting Abstracts*, volume 2017, pages H43G–1725.

Sangnimnuan, A., Li, J., and Wu, K. (2018). Development of efficiently coupled fluid- flow/geomechanics model to predict stress evolution in unconventional reservoirs with complex-fracture geometry. *SPE Journal*, pages 640–660.

Sasaki, T. and Rutqvist, J. (2021). Estimation of stress and stress-induced permeability change in a geological nuclear waste repository in a thermo-hydrologically coupled simulation. *Computers and Geotechnics*, 129:103866.

Selvadurai, A. and Selvadurai, P. (2010). Surface permeability test: experiments and modelling for estimating effective permeability. *Proceedings of the Royal Society A*, 466:2819– 2846.

Showalter, R. E. (2000). Diffusion in Poro-Elastic Media. *Journal of Mathematical Analysis and Applications*, 251(1):310–340.

Takahashi, M., Park, H., Takahashi, N., and Fujii, Y. (2013). True triaxial tests - using permeability and extensional stress parameters to simulate geological history in rocks. *Geosystem Engineering*, 16(1):75–82.

Terzaghi, K. (1923). Die Berechnung der Durchlassigkeitsziffer des Tones aus dem Verlauf der Hydrodynamichen Spannungserscheinungen Akademie der Wissenschaften in Wien. *Mathematish-Naturwissen-Schaftiliche Klasse*, 132:125–138.

Terzaghi, K. (1925). *Erdbaumechanik auf Bodenphysikalischen Grundlagen*. Leipzig u. Wien, F. Deuticke.

Touhidi-Baghini, A. (1998). *Porosity reduction and crustal pore pressure development*. PhD thesis, Department of Civil Engineering, University of Alberta.

Vadillo-Sáenz, M., Aguilar-Gastelum, P., Díaz-Viera, M., and Coronado, M. (2020a). Permeability simulation in an elastic deformable sandstone under stress changes. *Suplemento de la Revista Mexicana de Física*.

Vadillo-Sáenz, M., Díaz-Viera, M., Coronado, M., and Aguilar-Gastelum, P. (2022). An analysis of standard permeability stress - dependent relationships in homogeneous elastic porous media. *Journal of Rock Mechanics and Geotechnical Engineering (submitted)*.

Vadillo-Sáenz, M., Domínguez-Torres, A., Díaz-Viera, M., Serrano-Saldaña, E., and Coronado, M. (2020b). Modelado de pruebas de flujo con deformación en roca caliza Bedford. *Internal Report of th Fondo Sectorial Conacyt Sener Hidrocarburos Project 280097 (IMP-Y.61066) October 15, 2020*.

Walder, J. and Nur, A. (1984). Porosity reduction and crustal pore pressure development. *Journal of Geophysical Research: Solid Earth*, 89(B13):11539–11548.

Wang, F., Sun, Z., Liu, H., Xu, T., and Jing, J. (2016). Experimental study on the variation of permeability of medium-fine feldspar-quartz sandstone low-permeability reservoir under the circulatory increasing or reducing conditions of confining pressure. *Geofluids*, 47:1125–1132.

Zhu, W., Montesi, L. G., and fong Wong, T. (1997). Shear-enhanced compaction and permeability reduction: Triaxial extension tests on porous sandstone. *Mechanics of Materials*, 25(3):199–214.

Zhu, W. and Wong, T.-f. (1997). The transition from brittle faulting to cataclastic flow: Permeability evolution. *Journal of Geophysical Research: Solid Earth*, 102(B2):3027–041.

Appendix A. Poroelastic Model Fitting of Hydrostatic and Non-Hydrostatic Compression Tests

In this appendix the fitting results of the experimental pressure drop data obtained from the non-hydrostatic and hydrostatic compression tests described in this paper are shown. They are graphically illustrated in Figures 9 and 10, respectively.
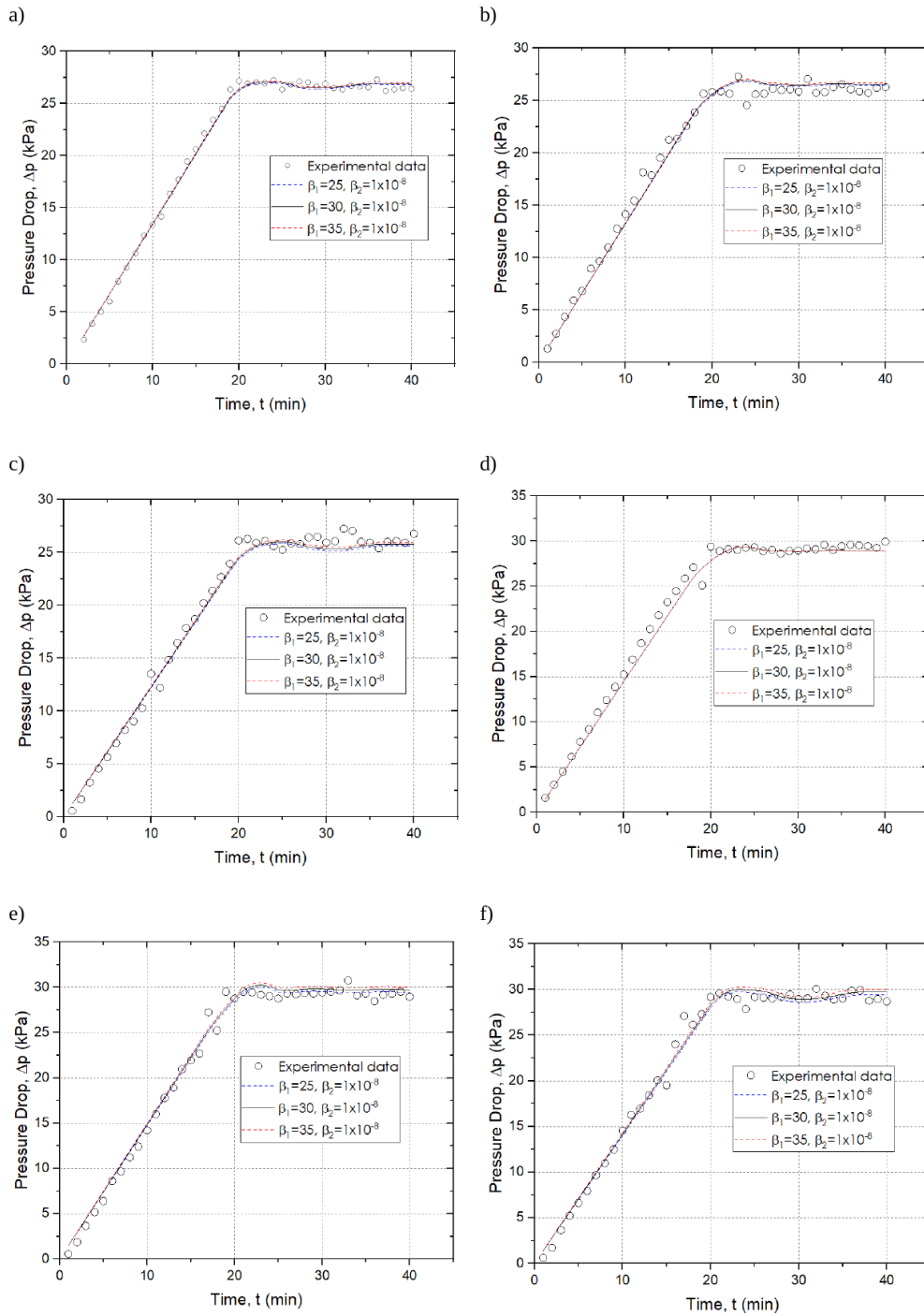

Figure 9. Pressure drop along the time for non-hydrostatic compression tests at confining stress: a) 12.4 MPa, b) 13.8 MPa, c) 19.3 MPa, d) 22.1 MPa, e) 24.8 MPa and f) 27.6 MPa. In hollow circles the experimental data and as broken lines the fitting curves corresponding to three different β_1 parameter values. Here, β_1 is dimensionless and β_2 has dimensions of 1/Pa.
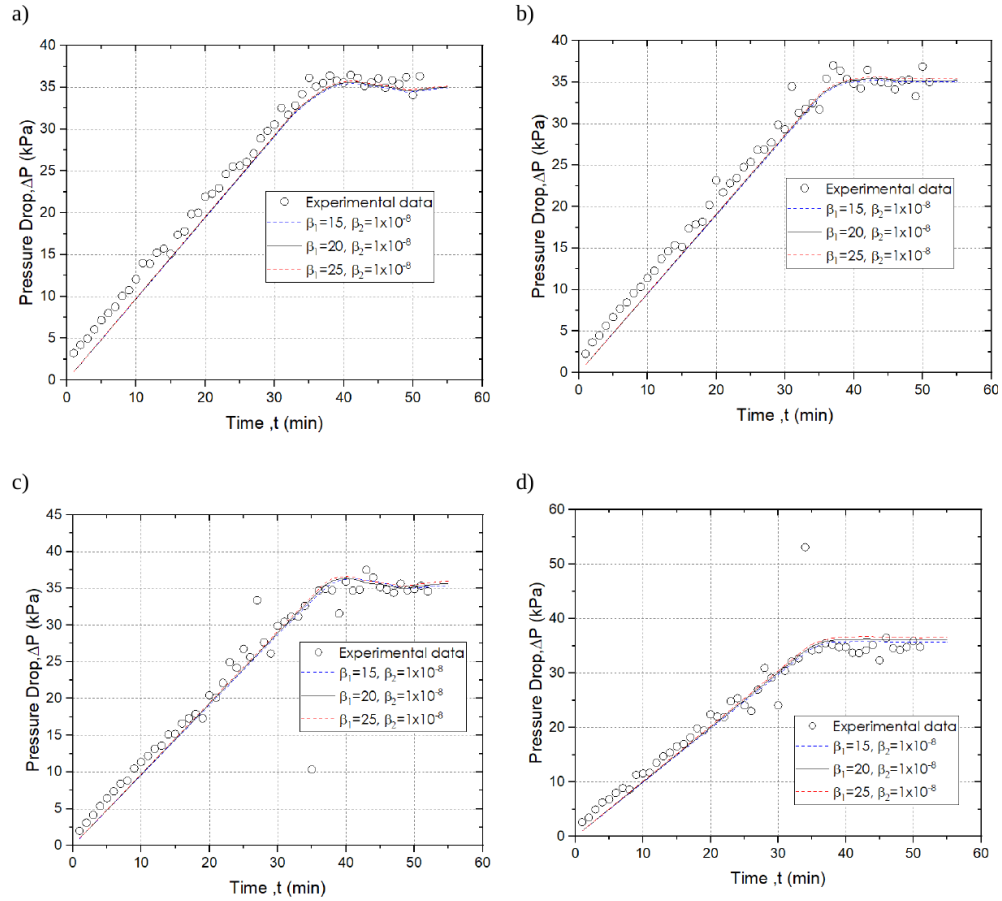
Figure 10. Pressure drop along the time for hydrostatic compression tests at confining stress: a) 10.3 MPa, b) 13.8 MPa, c) 20.7 MPa and d) 27.6 MPa. In hollow circles the experimental data and as broken lines the fitting curves corresponding to three different β_1 parameter values. Here, β_1 is dimensionless and β_2 has dimensions of 1/Pa.